Nanoscale

Accepted Manuscript

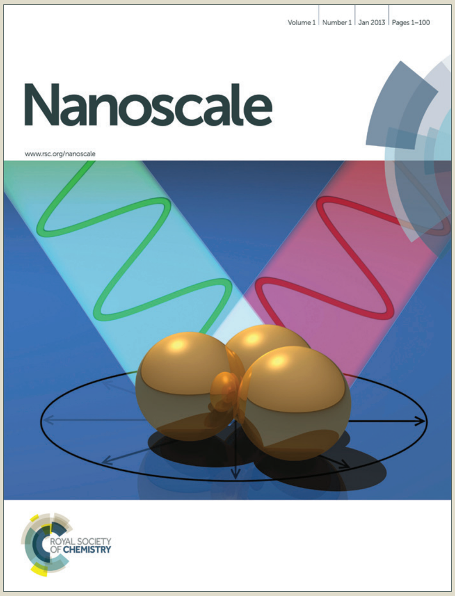

This is an *Accepted Manuscript*, which has been through the Royal Society of Chemistry peer review process and has been accepted for publication.

Accepted Manuscripts are published online shortly after acceptance, before technical editing, formatting and proof reading. Using this free service, authors can make their results available to the community, in citable form, before we publish the edited article. We will replace this *Accepted Manuscript* with the edited and formatted *Advance Article* as soon as it is available.

You can find more information about *Accepted Manuscripts* in the Information for Authors.

Please note that technical editing may introduce minor changes to the text and/or graphics, which may alter content. The journal's standard Terms & Conditions and the Ethical guidelines still apply. In no event shall the Royal Society of Chemistry be held responsible for any errors or omissions in this *Accepted Manuscript* or any consequences arising from the use of any information it contains.

ROYAL SOCIETY OF CHEMISTRY

www.rsc.org/nanoscale

Journal Name RSCPublishing

ARTICLE

Cite this: DOI: 10.1039/x0xx00000x

Received 00th January 2012,

Accepted 00th January 2012

DOI: 10.1039/x0xx00000x

www.rsc.org/

Towards a unified description of the charge transport mechanisms in conductive atomic force microscopy studies of semiconducting polymers

D. Moerman,[a] N. Sebaihi,[a] S. E. Kaviyil,[c] P. Leclère,[a] R. Lazzaroni[ab]
O. Douhéret,[*b]

In this work, conductive atomic force microscopy (C-AFM) is used to study the local electrical properties in thin films of self-organized fibrillate poly(3-hexylthiophene) (P3HT), as a reference polymer semiconductor. Depending on the geometrical confinement in the transport channel, the C-AFM current is shown to be governed either by the charge transport in the film or by the carrier injection at the tip-sample contact, leading to either bulk or local electrical characterization of the semiconducting polymer, respectively. Local I-V profiles allow to discriminate the different dominating electrical mechanisms, i.e., resistive in the transport regime and space charge limited (SCLC) in the local regime. A modified Mott-Gurney law is analytically derived for the contact regime, taking into account the point-probe geometry of the contact and the radial injection of carriers. Within the SCLC regime, the probed depth is shown to remain below 12 nm with a lateral electrical resolution below 5 nm. This confirms that high resolution is reached in those C-AFM measurements, which therefore allows for the analysis of single organic semiconducting nanostructures. The carrier density and mobility in the volume probed under the tip in steady-state conditions are also determined in the SCLC regime.

1 Introduction

Within the last decade, novel electronic components based on organic semiconductors have emerged, driven by the prospect of fabricating devices on large-area substrates at low cost[1]. A steady increase in the performances relies on the tailoring of the material properties, combined with a thorough understanding of the physical mechanisms at play in the devices, in particular charge generation/injection and charge transport.

Because the microscopic morphology of the active layers strongly influences those physical processes, high-resolution scanning probe techniques are of prime importance for further material and device improvement, especially in organic photovoltaic cells (OPV), where intimate contact, large density of interfaces and efficient percolation paths are required for efficient exciton dissociation and charge transport. Conductive atomic force microscopy (C-AFM) and related methods have been successfully applied to analyse the local electrical properties of the materials and structures composing the OPV photoactive layers[2-13]. Combining non-destructive analysis (with contact forces in the nanoNewton range) and high spatial resolution (< 10 nm), these methods exhibit sufficiently high current sensitivity (< 100 fA) to access the typical electrical response of organic semiconductors upon moderate dc bias (a few V).

Specific C-AFM studies of semiconducting polymer films have brought major understanding on the transport properties through local space charge limited current (SCLC) behaviors recorded by local I-V profiles[3-8,12]. C-AFM measurements are carried out either in top (or diode, out-of-plane) configuration with the back electrode located hundreds of nm beneath the scanned area, or in lateral (or in-plane) configuration with the back electrode hundreds of µm far from the tip. For instance Ginger's group has been the first to extract reliable values of charge carrier mobility from the C-AFM measurements[5]. This was achieved by correlating macroscopic SCLC measurements (in diode configuration) with C-AFM I-V profiles (where the C-AFM tip replaces one of the two macroscopic electrodes), supported by finite element simulations. They proposed a modified Mott-Gurney law with semi-empirical scaling factors and took into account the point probe geometry for the injection electrode and the thickness of the film (the distance between the C-AFM tip and the back contact electrode).

---

[a] Laboratory for Chemistry of Novel Materials, Center for Innovation and Research in Materials and Polymers - CIRMAP, University of Mons - UMONS, Place du Parc 20, B-7000 Mons, Belgium;
[b] Materia Nova Materials R&D Center, Avenue Nicolas Copernic 1, B-7000 Mons, Belgium;
[c] Department of Materials Science, University of Milano-Bicocca, Via R. Cozzi 53, 20125 Milan, Italy

*Corresponding author e-mail: olivier.douheret@materianova.be

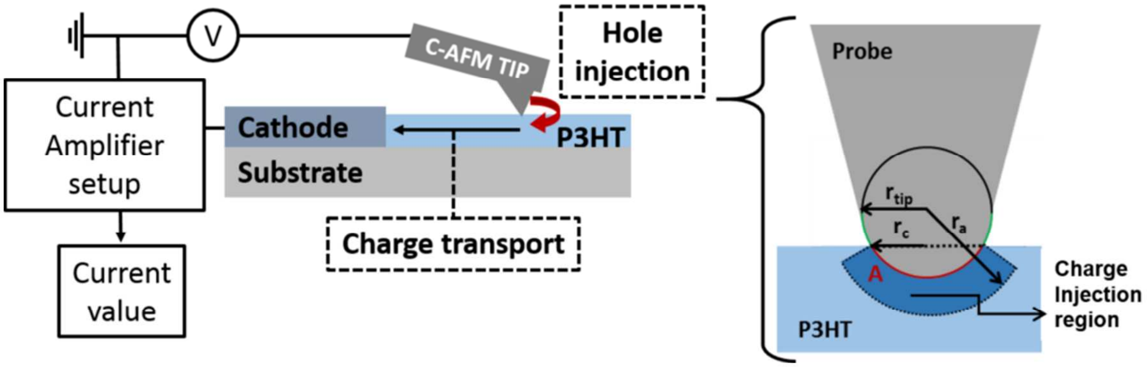

Figure 1: Schematic representation of the side scanning C-AFM configuration, highlighting the two major mechanisms involved in the measurement: the hole injection occurring at the tip-sample contact (right part) and the charge transport through the semiconducting layer to the cathode.

Desbief et al.[6] have qualitatively studied similar semiconducting films but in a lateral configuration (cf. Fig. 1 left). C-AFM I-V profiles also exhibit a SCLC-like behaviour but, unlike Ginger's observations, the C-AFM current intensity was shown to be independent on the distance to the back contact electrode, demonstrating the local character of the C-AFM measurements in this specific experimental configuration. Bolsée et al.[7], and Sengupta et al.[14] independently studied the electrical properties of isolated semiconducting organic nanofibres, in the lateral configuration. Unlike Desbief et al., the electrical response was shown to depend on the back contact distance.

This work aims at overcoming this apparent discrepancy in the results, by providing a global description of the mechanisms ruling the charge transport in semiconducting polymers, when studied with C-AFM. It is based on the analysis of the effects of geometrical confinement of the transport on the electrical properties in thin films of a prototypical polymer semiconductor, poly(3-hexylthiophene) (P3HT). This material is widely used in OPVs, as the electron-donating, hole-transporting component. The nanoscale fibrillate organization of P3HT in thin films (see Supporting Information (SI) 1) is shown to yield high carrier mobility (0.3 and 0.7 $cm^2\ V^{-1}.s^{-1}$ in OFET configuration[15]) endowed by π-stacking of the polymer chains[16,17]. By measuring the C-AFM response along transport channels with a well-defined geometry, different charge transport mechanisms are identified in this work. In the so called contact-dominating regime, the space charge limited current is described analytically taking into account the specific geometry of the point contact. This leads to high-resolution characterization of the electrical properties, including the mobility and the carrier density.

2 Experimental

The P3HT thin films were first obtained by drop casting from dilute solutions in chlorobenzene (0.2 mg.mL-1) on patterned glass/ITO substrates (R□=15 Ω.□), followed by slow solvent evaporation to favour the self-organization of the polymer chains into fibres. The concentration is set to yield partial coverage of the substrate by the P3HT deposit. In a second step, the protocol was modified to favour self-organization of the polymer chains in the solution, in order to fabricate fully fibrillate P3HT deposits with a uniform thickness, using spin-coating[8,18]. The C-AFM measurements were carried out in air using a Bruker Multimode microscope equipped with a Nanoscope V controller and an Extended TUNA external module for current detection. A $PtIr_5$ conductive coating on etched Si probes ensured good electrical contact at the tip-sample contact, while low spring constant and deflection set-point guaranteed low contact forces, preventing mechanical or electrical damage upon scanning. This also allowed the determination of the radius of the mechanical contact, as discussed below. The work- function of ITO φ_{ITO} is around 4.7 eV[19] and that of the $PtIr_5$ tip φ_{Tip} is ~5.2 eV[20]. φ_{Tip} can vary with the experimental environment (gas adsorption, pillow effect…). Yet considering the low threshold voltages for hole injection, these variations can be ignored. In the electrical measurements, the tip is therefore the anode and ITO is the cathode. Since the HOMO of P3HT lies around 5.1 eV[21], the C-AFM current originates only from the transport of holes. The high value of φ_{Tip} also ensures that no injection barrier is in principle present at the tip-P3HT interface. Yet the C-AFM measurements have to be performed applying a negative dc sample bias above a threshold voltage (~300-500 mV[6-8]), which is likely to ensure appropriate band bending for the transport of holes injected from the probe into the sample and collected at the ITO cathode. Finally, a lateral scanning configuration is chosen, i.e., the tip scans the organic film over the bare glass substrate while the ITO back contact lies sideways, microns away from the analysed area, as presented in Figure 1. This configuration implies that two major mechanisms are likely to contribute to the C-AFM current: the injection of holes at the tip-sample contact and their transport throughout the mesh of P3HT fibres to the back electrode, as in Figure 1.

3 Results and discussion

Figures 2 (a) and (b) show typical height and current C-AFM images, respectively, of a dense mesh of P3HT fibres deposited on glass and electrically connected laterally to the ITO cathode. Bare glass regions (i.e., the lower part of the image) expectedly exhibit zero current, as is also the case for individual P3HT clusters that are not connected to the ITO. Current in the pico ampere range is measured not only on the whole mesh of fibres, but also along the isolated fibres protruding from the mesh, as highlighted in Figure 2 (c). Two different behaviours can be distinguished: (i) in the mesh, the value of the C-AFM current is almost constant, irrespective of the tip-ITO distance (see Figure 2 (d)), i.e., irrespective of the length of the path travelled by the carriers in the semiconductor. Here the maximum tip-ITO distance is 15 μm; similar observations of a constant current have been reported over tens, even hundreds of microns by Desbief et al.[6]; (ii) in contrast, along the single fibre the current decreases with the distance between the tip and the connection of the fibre with the mesh (see Figure 2 (e)). A similar behaviour has been reported by Bolsée et al. for single fibres individually connected to a metallic electrode in a scanning gate configuration[7]. In our opinion, these two different behaviours originate from the difference in the cross section of the transport path for the carriers. In the mesh, many conduction paths are available for the injected holes to the ITO, whereas in a single fibre, the holes can only travel along a narrow path until they reach the mesh. One can try to understand the effect of this difference by analysing the equivalent electrical circuit corresponding to the C-AFM measurement. Assuming: (i) no injection barrier at the tip-sample contact, (ii) an ohmic back contact at the ITO for hole collection and (iii) a low resistance for the external circuit, the resistances that set the current value can be restricted to: (i) the resistance of transport $R_{Transport}$ in the semiconductor thin film and (ii) the contact resistance $R_{Contact}$ induced by the constriction of current across the small-size tip-sample contact. We stress that, here, the contact appellation refers to local bulk electrical properties probed only underneath the tip sample contact (see deep blue area depicted in Fig. 1, right part), contrary to transport designation that indicates the contribution of the whole film in the electrical response. In the equivalent circuit, these two resistances are connected in series and the highest resistance sets the current intensity measured at a given dc bias. The transport resistance can be expressed as:

$$R_{Transport} = \rho_{Film} \frac{L}{w.t} \qquad \text{(Eq. 1)}$$

with ρ_{Film} the resistivity of the film, L distance between the tip and the ITO, t the thickness of the film and w the film width. The contact resistance $R_{Contact}$ only depends on the local electrical properties of the semiconductor and the size of the tip-sample contact. In analogy with the spreading current mechanism described across an ohmic point contact in classical microelectronics[22], we propose the following expression:

$$R_{Contact} = \frac{\rho_{Local}}{\alpha.d} \qquad \text{(Eq. 2)}$$

with ρ_{Local} the resistivity of the film underneath the tip-sample contact, d a dimensional factor taking into account the size of the point probe contact, and α a dimensionless scalar related to the sphere-plane geometry of the contact. The ratio between the two resistances is given by:

$$\frac{R_{Transport}}{R_{Contact}} = \frac{\rho_{Film}}{\rho_{Local}} \frac{\alpha.d.L}{w.t} \qquad \text{(Eq. 3)}$$

At a fixed dc sample bias, the resistivity ratio can be considered as constant and variations of the resistance ratio can only be induced by the geometrical and dimension-related parameters. If $R_{Transport}$ dominates $R_{Contact}$, the C-AFM current is expected to hyperbolically decrease with L. Conversely the current is not expected to be affected by the length of the conduction path (i.e., the tip-electrode distance) if $R_{Contact}$ is the largest resistance. In the fiber mesh, considering the many conduction paths, w corresponds to the width of the ITO back contact, typically a few mm and $R_{Transport}$ is thus rather small; $R_{Contact}$ can therefore prevail and the current intensity is independent of the tip-ITO distance (as observed in Figure 2 (d)). In contrast, across a single fiber, w is the width of the fiber, i.e. ~30 nm, and $R_{Transport}$ can therefore increase by up to five orders of magnitude compared to the mesh. It is therefore reasonable to expect that $R_{Transport}$ is prevalent along the fiber, so that the measured current gradually decreases when the tip is moved along the fiber, away from the connection to the mesh, as illustrated in Figure 2 (e).

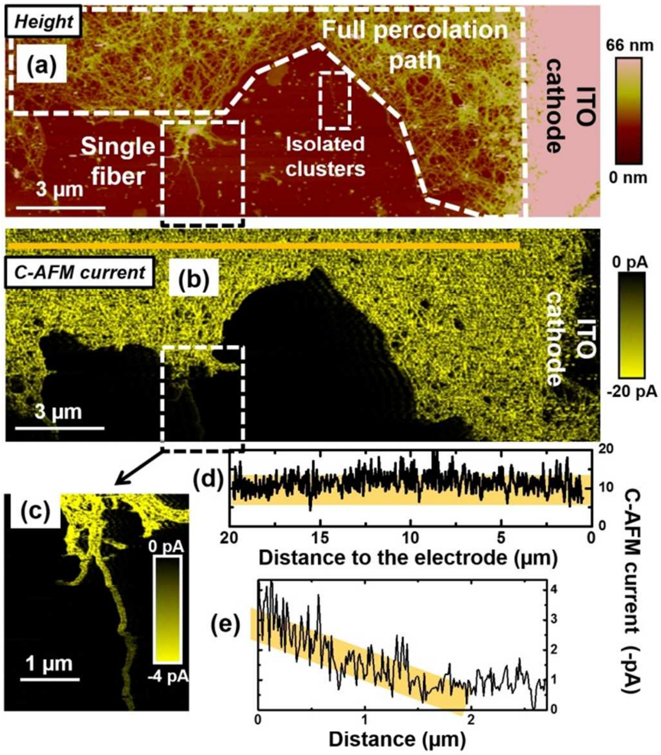

Figure 2 : (a) AFM height image obtained in contact mode on a fibrillate P3HT deposit on a glass substrate; the ITO electrode is located on the right side of the image. The corresponding C-AFM current image, obtained with a dc sample bias of -0.5 V, is shown in (b). (c) Zoom from image (b). (d) and (e) present the current profiles obtained along the yellow horizontal line in image (a) and along the long-axis of the fiber in image (c) respectively. In graph (d), the x-axis corresponds to the distance between the tip and the ITO electrode; in graph (e), it is the distance between the tip and the connection of the fiber to the continuous mesh.

To better determine the conditions in which either the transport-dominating or the contact-dominating regime acts, conducting channels with a well-defined width were generated in a continuous fibrillate thin film of P3HT in contact with an ITO electrode. This was done by scratching away the P3HT material down to the glass substrate with a diamond-coated AFM tip mounted on a stiff cantilever. Trenches were thus generated to separate P3HT zones of a selected width; constant zero current is recorded along those trenches, ensuring that the channels are electrically insulated from each other. Figure 3 (a) shows the C-AFM current image obtained with a dc sample bias of -1.2 V across three P3HT channels of different widths (w_1= 1.8 µm, w_2= 5.2 µm, w_3= 8.1 µm) and common length (L= 50 µm). Clear differences appear in the C-AFM current along those channels when moving away from the ITO electrode, which is located on the left-most side of the image. On both sides of the channels (i.e., on the top and bottom of the image) and beyond the end of the channels (i.e., in the area out of the image on the right side), the continuous P3HT film is connected to the ITO over a very large width (> 1 mm). On those zones, a constant current (~-80 pA) is measured, irrespective of the tip-ITO electrode distance, similar to what was observed on the mesh in Figure 2 (b). Because w is large, $R_{Transport}$ is relatively small and the current is in the contact-dominating regime. In contrast, in the channels, the current is observed to decrease with the separation from the ITO electrode. Most importantly, these decreases are not monotonous. When plotting the average current as a function of the tip-electrode distance, two different electrical regimes can be observed in the channels (Figure 3 (b)). For small tip-ITO distances, a constant

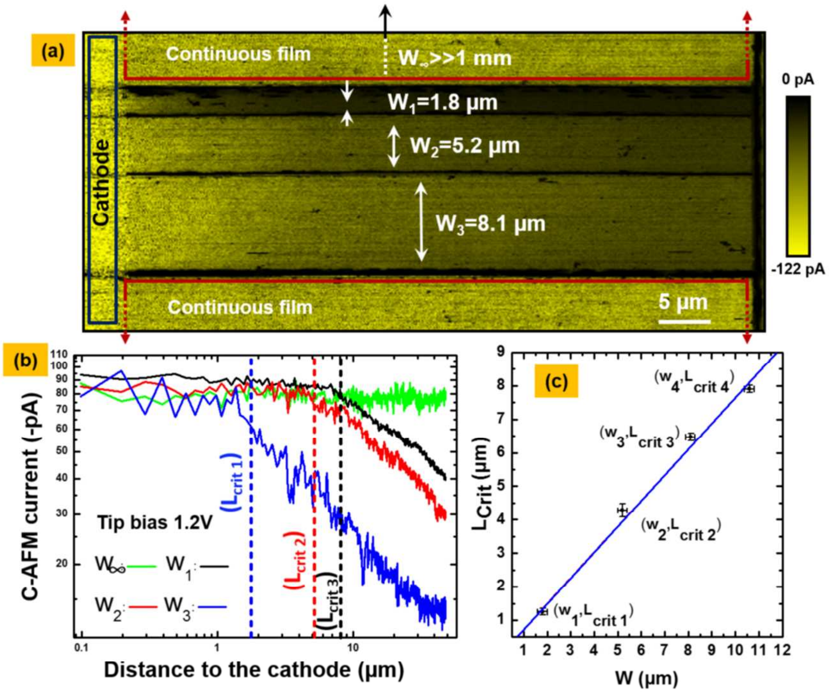

Figure 3: (a) C-AFM current image obtained with a dc sample bias of -1.2 V on a P3HT deposit patterned into three channels (W_1, W_2 and W_3) on the glass substrate next to the ITO cathode. (b) Current-distance profiles extracted from (a) along the axis of the channel. (c) Variation of the critical distance L_{crit} with the channel width. An additional experimental data point (W_4, $L_{crit\ 4}$) was measured on a wider channel not shown in image (a).

current is measured, with an intensity as high as that measured in the continuous film. As the tip-ITO distance increases, the current starts decreasing. This behavior can be explained in the following way: close to the electrode, L is small, so is $R_{Transport}$, and the current is therefore contact-dominated, i.e., independent of the distance. When moving away from the electrode, L is increasing and the contribution of the transport resistance to the current signal becomes dominant. These observations are qualitatively consistent with Eq. 3 relating high (low) L to the transport- (contact-) dominating regime.

The L-independent current observed close to the electrode is consistent with the contact-dominating regime described by Eq. 2. In the transport-dominating regime, the resistance is proportional to L (Eq. 1), so the current is inversely proportional to L and a slope value of -1 is expected in the log(I)-log(L) curves of Figure 3 (b). This is not the case: the value of the slope is actually -0.36, -0.42 and -0.49 for w_3, w_2, and w_1 respectively. This discrepancy is attributed to the geometry of these channels, for which a relatively small L/w ratio slows the increase of $R_{Transport}$ with L. Hence, a significant contribution from $R_{Contact}$ remains. An increase of the L/w ratio effectively leads to the expected -1 slope. The Log(I)-Log(L) profile evidencing independently the two regimes is given in SI 2, together with a fit taking into account the analytical expressions of the two resistances (Eq. 1 and 2) connected in series.

From the curves in Figure 3 (b), it is possible to define the tip-ITO distance from which the current starts to decrease along the channel (L_{crit}). This situation corresponds to $R_{Transport} = R_{Contact}$ and Eq. 3 can be modified as:

$$L_{Crit} = \frac{\rho_{Local}}{\rho_{Film}}.\frac{t}{\alpha.d}\,w \qquad \text{(Eq. 4)}$$

In Figure 3 (c), L_{crit} is plotted as a function of the channel width w; consistently with Eq. 4, a linear increase of L_{crit} with w is observed. This further confirms the identification of a transition between the two current regimes in the channels, dominated by the contact resistance close to the electrode and by the transport resistance away from the electrode.

Figure 4 (a) shows two I-V profiles recorded for a 12 nm-thick continuous film patterned into a 10.2 µm-wide channel. The voltage is monotonically increased as the probe scans across an area of the channel that is very small compared to the channel length. To maximize the signal to noise ratio, the I-V profile is then constructed by averaging every line of the scanned window. The blue I-V profile recorded far from the ITO cathode (L= 56 µm) is shown to be dominated by the transport resistance: a linear variation is observed, corresponding to a resistance $R_{transport}$~21 GΩ. This value is sufficiently high to neglect the contribution of the resistances from the ITO back contact and the external circuit, as previously assumed. Injecting the geometrical parameters in Eq. 1, this resistance value corresponds to ρ_{film}~4600 Ω.cm, i.e., a conductivity σ_{film}~2.2 10^{-4} $\Omega^{-1}.cm^{-1}$.

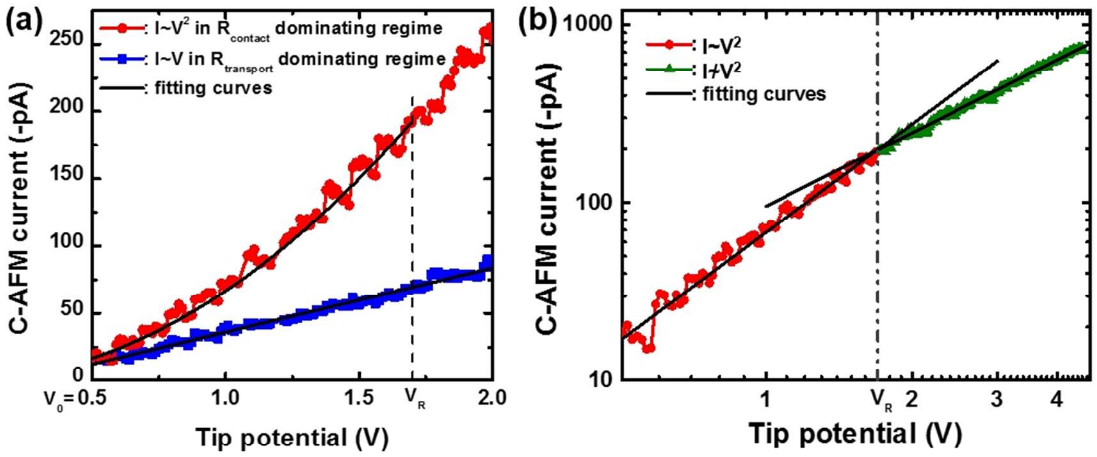

Figure 4: (a) Local I-V profiles obtained within a 10.2 µm-wide channel in the contact (red) and transport (blue) resistance dominating regimes on a 12 nm-thick film of fibrillate P3HT. The black lines correspond to the quadratic (red) and linear (blue) fit of the curves. (b) I-V profile in log-log scale in the contact resistance dominating regime from (a).

In the contact regime (i.e. close to the ITO electrode; red curve in Figure 4), quadratic variations of the current with the voltage are observed in the [V_0; V_R]=[0.5 V; 1.7 V] voltage range. These variations have been frequently reported in literature[3-6, 8, 12] and attributed to SCLC transport. This is likely to arise from charge accumulation in the sample locally underneath the probe and is therefore characteristic of lateral scanning configuration when contact resistance prevails. The spatial extension of the space charge limited current region (SCLCR), where such charge accumulation takes place, is here conditioned by the depth r_a-r_{tip} (see Figure 1-right) and r_c the contact radius. This defines the volume that is effectively probed leading to the measured C-AFM current, which reflects the more or less local nature of the C-AFM measurement.

The features of the SCLCR can depend on the geometry of the contact between the tip and the polymer film, and two typical situations can be considered: large indentation (Figure 5 (a)) or small indentation. The contact area between the tip and the sample increases with the indentation and the current is also expected to increase. If the current depends only on the extension of that area, simple geometrical considerations give the expected ratio of the current value between a half-buried hemispherical tip (as a model for strong indentation) and the small-indentation case:

$$I_{low\ forces} = \frac{{r_c}^2}{2{r_{tip}}^2} I_{half\ buried\ tip\ apex} \qquad \text{(Eq. 5)}$$

with r_c defining the radius of the spherical cap in contact with the sample. The small-indentation case is therefore related to $r_c \ll r_{tip}$.

For large indentation, considering a hemispherical tip apex half-buried in the polymer film (Figure 5 (a)), the analytical I-V expression of SCLC transport beneath the probe can be analytically derived by solving Poisson’s equation (Eq. 6) with Ohm’s law (Eq. 7) in spherical coordinates:

$$\vec{\nabla} \cdot \vec{E} = \frac{1}{r^2}\frac{\partial (r^2 E_r)}{\partial r} = \frac{ep}{\varepsilon_r \varepsilon_0} \qquad \text{(Eq. 6)}$$

$$I = 2\pi e \mu p r^2 E_r \qquad \text{(Eq. 7)}$$

with p and µ the free carrier density and mobility, respectively. In steady-state conditions, I is constant. Combining Eq. 6 and 7, using the center of the apex of the tip as the origin, and integrating between r_{tip} (the tip radius) and r, one obtains the analytical expression of the radial field E_r with r:

$$E_r = \sqrt{\frac{I}{3\pi \varepsilon_r \varepsilon_0 \mu}} \cdot \sqrt{\frac{r^3 - {r_{tip}}^3}{r^4}} \qquad \text{(Eq. 8)}$$

The derivation of Eq. 7 and the details of the derivations of the following equations, including the contribution of the geometry of the soft probe-sample contact, are given in SI 3. Since:

$$E_r = -\frac{\partial V}{\partial r} \qquad \text{(Eq.9)}$$

the Mott-Gurney law for a point probe configuration can be derived, integrating Eq. 8 over r between r_{tip} and r_a. At this stage, we have no clue on the spatial extension of the charge accumulation zone. We will thus consider two extreme cases: a very large accumulation zone or a very small one (represented by r_{a1} and r_{a2}, respectively, in Figure 5 (a)). The analytical solution for the former case ($r_{tip} << r_{a1}$) is described in SI 3, approximation 1. Consistently with well-known theoretical derivations[23], one obtains:

$$I = \frac{3\pi}{4} \varepsilon_r \varepsilon_0 \mu \frac{1}{r_a} V^2 \qquad \text{(Eq.10)}$$

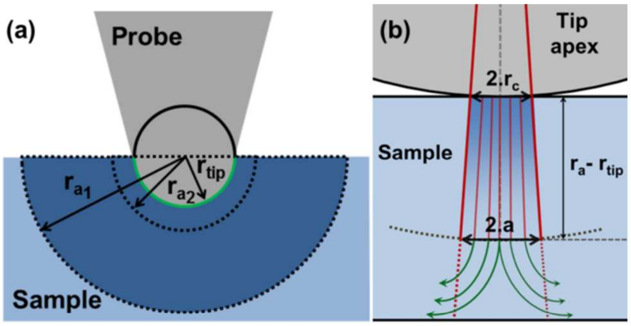

Figure 5: Schematic representation of the tip-sample contact, with (a) a large probe indentation (half-buried sphere) and (b) a more realistic case of small indentation, in lateral configuration, i.e., with a back electrode located sideways and far away from the local injecting point contact.

For the latter case, i.e., $r_{a2} \gtrsim r_{tip}$ (Approximation 2 in SI 3), Eq. 7 can be modified into:

$$E_r \approx \sqrt{\frac{2.I}{\pi\epsilon_0\epsilon_{r\mu}}}\sqrt{\frac{r-r_{tip}}{r_c^2}} \qquad \text{(Eq.11)}$$

Again, consistently with the literature [23], integrating E_r from r_{tip} to r_a now yields:

$$I = \frac{9}{8}\epsilon_0\epsilon_r\mu\frac{2\pi r_{tip}^2}{\left(r_a - r_{tip}\right)^3}V^2 \qquad \text{(Eq.12)}$$

This expression actually corresponds to the standard Mott-Gurney law in planar configuration. This is because when r_a and r_{tip} are sufficiently close to one another, the probed volume is located between two concentric hemispheres of similar radius, which can be expected to behave like two parallel planes.

For small indentation (Figure 5 (b)), the expressions of the current can be deduced from the combination of equation 5 and equations 10 and 12. This yields:

$$I = \frac{3\pi}{8}\varepsilon_r\varepsilon_0\mu\frac{r_c^2}{r_{tip}^2 r_a}V^2 \quad \text{for the large } r_a \text{ case} \qquad \text{(Eq.13)}$$

$$I = \frac{9\pi}{8}\epsilon_0\epsilon_r\mu\ \frac{r_c^2}{\left(r_a - r_{tip}\right)^3}V^2 \quad \text{for the small } r_a \text{ case} \qquad \text{(Eq.14)}$$

In the typical experimental conditions applied in the present C-AFM measurements, the force applied by the tip was maintained below ~1.2 nN. This upper limit for the applied force is obtained from a spring constant of the cantilever ~0.26 N/m (determined by thermal tune) and a cantilever deflection ~4.5 nm (measured by means of the photo detector). The maximum contact radius r_c and the indentation can then be estimated from the Hertz model, i.e. assuming fully elastic deformation of the polymer. With a 25 nm radius for the tip apex and a Young Modulus ~1 GPa for P3HT [7], the contact radius and the indentation are estimated to be below 2.7 nm and 0.15 nm, respectively. This clearly corresponds to a small indentation situation and equations 13 and 14 are the relevant ones for describing the SCLC regime.

Irrespective of the size of the probed volume (i.e., the value of r_a), quadratic variations of the current with the voltage are expected from those equations, as in the standard Mott-Gurney law. A quadratic increase of the current with the contact radius r_c is also predicted, consistently with an increase of the contact surface as the tip further penetrates in the polymer when a larger load is applied (while remaining in the small indentation regime). When considering: (i) "the large r_a approximation" (Eq. 13), (ii) μ in the [0.01; 0.001] cm²/V.s range (as usually reported in literature for fibrillate P3HT [5,7,15,17], (iii) r_c in the [1; 3] nm range, and (iv) the [1 V; 90 pA] voltage-current set of values (extracted from the I-V profile), one obtains unrealistically small values of r_a, in the [0.06; 5] nm range, which shows the inadequacy of that approximation. In the approximation of a small r_a (Eq. 14), the same μ, $r_,$ I and V values yield an estimate of $r_a - r_{tip}$ in the [4.8; 21.6] nm range, which is more realistic and consistent with the hypothesis supporting this case. Henceforth, Eq. 14 will be considered as appropriate for further determination of the local electrical parameters below.

First, Eq. 14 can be used to determine the carrier mobility μ, in the probed volume upon steady state current flow, since,

$$\mu = \frac{8}{9\pi}.\frac{10^B}{\varepsilon_r\varepsilon_0}.\frac{\left(r_a - r_{tip}\right)^3}{{r_c}^2} \qquad \text{(Eq.15)}$$

with B experimentally determined by the parabolic fitting of the curve in Fig. 4, such as log (I) = 2log (V) + log (B). The carrier density $p_{cont}(r)$ in the SCLCR can also be determined from the combination of Ohm's law, Eq. 7 and Eq. 14, as follows:

$$p_{cont}(r) = \frac{3}{4}.\frac{\varepsilon_r\varepsilon_0}{e}.\frac{1}{\left(r_a - r_{tip}\right)^{3/2}}.\frac{1}{\left(r - r_{tip}\right)^{1/2}}.V \qquad \text{(Eq.16)}$$

All the details of the analytical derivations are given in SI 3. Between r_{tip} and r_a, $p_{cont}(r)$ monotonically decreases, moving away from the tip-sample interface, consistently with a local carrier accumulation.

The estimates of the mobility and the charge density strongly depend on (r_a - r_{tip}) (in other words on the extension of the SCLCR) and also rely on an accurate estimation of the electrical contact radius r_c. To determine them experimentally and independently, we consider a set of boundary conditions. Eq. 16 indicates that charges accumulate in the probed volume underneath the tip apex with a depth extension r_a - r_{tip}. The first boundary condition (B.C. 1) is the charge continuity between the probed volume and the bulk of the film: $p_{cont}(r = r_a) = p_{film}$ irrespective of the voltage in the SCLC regime. Therefore B.C. 1 can be developed as:

$$p_{film} = p_{cont}(r = r_a) = \frac{3}{4}.\frac{\varepsilon_r\varepsilon_0}{e}.\frac{1}{\left(r_a - r_{tip}\right)^2}.V$$

$$\Leftrightarrow\ r_a - r_{tip} = \sqrt{\frac{3}{4}.\frac{\varepsilon_r\varepsilon_0}{e}.V.\frac{1}{p_{film}}} \qquad \text{(Eq. 17 = B.C. 1)}$$

r_a - r_{tip} logically increases with the voltage in which the SCLC regime prevails. Similarly to p_{cont}=p_{cont}(V) from Eq. 16, μ=μ(V) can be derived from Eq. 15 and Eq. 17:

$$\mu = \frac{1}{\sqrt{3}\pi}.\frac{10^B}{{p_{film}}^{3/2}}.\frac{\sqrt{\varepsilon_r\varepsilon_0}}{e^{3/2}}\frac{1}{{r_c}^2}V^{3/2} \qquad \text{(Eq.18)}$$

Both $p_{cont}(r)$ and μ are logically shown to increase with the voltage. At V = V_0 the mobility satisfies the continuity in the carrier mobility, i.e. B.C. 2: $\mu(V = V_0) = \mu_{film}$.

Finally for V > V_R, the I-V profile exhibits a linear variation (Figure 4 (b)), indicating that the SCLC regime no longer dominates the charge transport. Similarly to the SCLC dominating regime, this resistive regime is not affected by the tip-counter electrode distance, indicating the local character of the dominating transport mechanisms. The small size of the contact is supposed to induce a spreading effect due to the constriction of the current lines. The spreading resistance R_S for a sphere-plane contact geometry with radial injection of the current at the contact usually satisfies Eq. 19, where *a* is the radius of the surface where the spreading effect occurs[22].

$$R_S = \frac{\rho_{film}}{4a} \qquad \text{(Eq.19)}$$

In the present case, charges are injected radially with a very small contact radius compared to the tip radius (1 ≤ r_c ≤ 3 nm; r_{tip} ≈ 25 nm). Consequently, the charge accumulation region generated below the probe cannot spread out broadly in the film. The spreading effect is therefore expected to take place beyond r= r_a (as illustrated in Figure 5 (b)) where charges are injected from the SCLCR into the bulk of the film. B.C. 3 implies R_S=$R_{Contact}$(V=V_R) thus leading to eq. 20.

$$R_S = \frac{\rho_{film}}{4\,r_c}\frac{r_{tip}}{r_a(V = V_R)} \qquad \text{(Eq. 20 = B.C. 3)}$$

B.C. 1, 2 and 3 define a three-equation system in which the three unknowns are r_c, μ_{film} and p_{film}. From the experimentally determined Rs (4.7 GΩ), ρ_{film} (4600 Ω.cm) and 10^B (8.71 10^{-11} A.V^{-2}), r_c and *a* are estimated to be 1.66 and 2.46 nm (at V=V_R), respectively. This confirms the high lateral resolution of the AFM electrical measurements. p_{film} and μ_{film} yield values of 1.58 10^{18} cm^3 and 8.69 10^{-4} $cm^2.V^{-1}.s^{-1}$, respectively, consistent with macroscopic values from the literature [5,7,15,17,24-26] and further confirming the validity to this local model.

The estimated values of r_a-r_{tip} in the SCLC voltage range are collected in Table 1 for three representative voltages: 0.5 V and 1.7 V are the limits of the SCLC range and 1.2 V is the value used for the measurements of Figure 3. The average carrier density $<p_{cont}>$ in the SCLCR is also displayed in Table 1. According to Eq. 21, $<p_{cont}>$ appears to be voltage independent.

$$\langle p_{cont}\rangle = \frac{1}{r_a - r_{tip}}\int_{r_{tip}}^{r_a} p_{cont}(r).dr$$

$$\Leftrightarrow \frac{3}{4}.\frac{\varepsilon_r\varepsilon_0}{e}.\frac{1}{\left(r_a - r_{tip}\right)^2}.V = 2p_{film} \qquad \text{(Eq. 21)}$$

Table 1: r_a-r_{tip}, μ and $<p_{cont}>$ values for three different voltages in the [0.5 V; 1.7 V] range.

V (V)	0.5	1.2	1.7
r_a-r_{tip} (nm)	6.51	10.08	12.00
μ ($cm^2.V^{-1}.s^{-1}$)	8.69 10^{-4}	3.23 10^{-3}	5.45 10^{-3}
$<p_{cont}>$ (cm^{-3})		3.14 10^{18}	

Within the whole SCLC voltage range, the accumulation depth r_a-r_{tip} lies below 12 nm. This is rather small, and combined with the experimentally determined values of r_c and a, this strongly confirms the ability of C-AFM to electrically characterize organic semiconducting structures on the nanoscale. This is of particular relevance for semiconducting blends such as those used in OPV devices, where the nanoscale organization is crucial for optimal performances. The intrinsic hole mobility estimated with this approach is consistent with the values frequently reported in literature for P3HT. In the SCLC voltage range, the mobility that is locally probed increases with the voltage by less than one order of magnitude. The dependence of μ with the electric field and the carrier density has been observed and intensively discussed [24,27]. In the present case, the increase we measure in the hole mobility appears to result rather from the higher electric field than from the rise of the carrier density. We find that the average carrier density $<p_{cont}>$ remains constant with the voltage (Table 1), because the increase in the number of carriers in the probed volume is compensated by the increase of r_a-r_{tip}. The intrinsic carrier density p_{film} of 1.57 10^{18} cm^{-3} derived is also consistent with the literature [24-26].

4 Conclusions

In this work the origin of the current in C-AFM measurements has been studied on fibrillate P3HT as a reference polymer semiconductor, with the aim of conciliating the typical but markedly different electrical behaviors reported in the literature. Depending on the confinement of the conducting channel, two electrical regimes are evidenced, in which the current is controlled either by the tip-sample contact or by the charge transport in the semiconductor. The I-V profiles recorded in both regimes confirm the origin of the C-AFM current, exhibiting resistive and space charge limited currents in transport and contact regimes, respectively. In the contact regime, the modified Mott-Gurney law for SCLC in a point-probe injection geometry and low contact forces has been analytically derived. The depth of the probed volume, the local carrier mobility, and the local carrier density in steady-state conditions have been determined for different voltages. In the SCLC regime, the operating voltage is to be chosen close to V_0, since this guarantees that the μ value that is extracted from the measurements is close to its intrinsic level. With low nN contact forces, these operating conditions also combine the smallest probed volume with low contact radius for optimal spatial resolution. Finally, this study underlines the capability of C-AFM to electrically resolve small-size organic semiconducting nanostructures, contributing to further understanding the local electrical properties and mechanisms in those materials.

Acknowledgements

This work was supported by the European Commission and Région Wallonne FEDER program (‘Revêtements fonctionnels’-SMARTFILM), the Science Policy Office of the Belgian Federal Government (BELSPO-PAI VII/5), the OPTI2MAT program of Région Wallonne and FNRS-FRFC. D.M. is grateful to FRIA for a doctoral fellowship. Ph. L. is a research associate of FNRS.

Notes and references

Electronic Supplementary Information (ESI) available:

SI-1: Tapping mode AFM image of fibrillar P3HT.

SI-2: Current-distance profile of a high aspect ratio channel exhibiting the both contact and transport resistance dominating regimes.

SI-3: Full analytical derivation of the Mott-Gurney law, describing SCLC regime in a point probe geometrical configuration for C-AFM measurements.

See DOI: 10.1039/b000000x/

1 S.R. Forrest, *Nature*, 2004, **428**, 911-918.

2 A. Alexeev, J. Loos, M. M. Koetse, U*ltramicroscopy,* 2006, **106** (3), 191–199.

3 O. Douhéret, L. Lutsen, A. Swinnen, M. Breselge, K. Vandewal, L. Goris, J. Manca, *Appl. Phys. Lett.,* 2006, **89** (3), 032107 (1-3).

4 O. Douhéret, A. Swinnen, M. Breselge, I. Van Severen, L. Lutsen, D. Vanderzande, J. Manca, *Microelectron. Eng.*, 2007, **84** (3), 431-436.

5 O. G. Reid, K. Munechika, D. S. Ginger, *Nano Letters*, 2008, **8** (6), 1602-1609.

6 S. Desbief, N. Hergué, O. Douhéret, M. Surin, P. Dubois, Y. Geerts, R. Lazzaroni, P. Leclère, *Nanoscale*, 2012, **4**, 2705-2712.

7 J.-C. Bolsée, W. D. Oosterbaan, L. Lutsen, D. Vanderzande, J. Manca, *Adv. Funct. Mater.*, 2012, **23** (7), 862-869

8 D. Moerman, R. Lazzaroni, O. Douhéret, *Appl. Phys. Lett.* 2011, **99**, 093303.

9 P. Willot, J. Steverlynck, D. Moerman, P. Leclère, R. Lazzaroni, G. Koeckelberghs, *Polym. Chem.*, 2013, **4**, 2662-2671

10 (a) A. Liscio, V. Palermo, P. Samori, *Adv. Funct. Mater.*, 2008, **18**, 907-914; (b) R. Berger, A. L. Domanski, S. A. L. Weber, *European Polymer Journal*, 2013, **19** (8), 1907-1915.

11 M. Osaka, H. Benten, L.-T. Lee, H. Ohkita, S. Ito, *Polymer*, 2013, **54**, 3443-3447.

12 J. Sun, K. Pimcharoen, S. R. Wagner, P. M. Duxbury, P. Zhang, *Organic Electronics*, 2014, **15**, 441-448.

13 (a) D. C. Coffey, O. G. Reid, D. B. Rodovsky, G. P. Bartholomew, D. S. Ginger, *Nano Letters,* 2007, **7** (3), 738-744; (b) L. S. Pingree, O. G. Reid, D. S. Ginger, *Nano Letters,* 2009, **21** (1), 19-28; (c) X.-D. Dang, A. Mikhailovsky, T.-Q. Nguyen, *App. Phys. Lett.*, 2010, **97** (11), 113303-3; (d) X.-D. Dang, A. B. Tamayo, J. Seo, C. V. Hoven, B. Walker, T.-Q. Nguyen, *Adv. Func. Mat.*, 2010, **20** (19), 3314-3321 ; (e) M. Guide, X.-D. Dang, T.-Q. Nguyen, *Adv. Mater.* 2011, **23** (20), 2313-2319; (f) W. C. Tsoi, P. G. Nicholson, J. S. Kim, D. Roy, T. L. Burnett, C. E. Murphy, J. Nelson, D. D. C. Bradley, J.-S. Kim, F. A. Castro, *Energy & Environmental Science,* 2011, **4** (9), 3646-3651; (g) B. H. Hamadani, N. Gergel-Hackett, P. M. Haney, N. B. Zhitenev, *Journal of Applied Physics,* 2011, **109** (12), 124501-7; (h) K. Maturová, R. A. J. Janssen, M. Kemerink, *ACS Nano*., 2010, **4**, 1385-1392.

14 S. Sengupta, D. Ebeling, S. Patwardhan, X. Zhang, H. von Berlepsch, C. Böttcher, V. Stepanenko, S. Uemura, C. Hentschel, H. Fuchs, F. C. Grozema, L. D. Siebbeles, A. R. Holzwarth, L. Chi, F. Würthner, *Angew. Chem. Int. Ed.* 2012, **51**: 6378–6382.

15 (a) S. Cho, K. Lee, J. Yuen, G. Wang, D. Moses, A. J. Heeger, M. Surin, R. Lazzaroni, *J. Appl. Phys.*, 2006, **100** (11); (b) M. J. Panzer, C. D. Frisbie, *Adv. Func. Mater.* 2006, **16**, 1051-1056.

16 W. D. Oosterbaan, J.-C. Bolsée, A. Gadisa, V. Vrindts, S. Bertho, J. D'Haen, T. J. Cleij, L. Lutsen, C. R. McNeill, L. Thompsen, J. Manca, D. Vanderzande, *Adv. Funct. Mater.*, 2010, **20** (5), 792-802.

17 H. Sirringhaus, P. J. Brown, R. H. Friend, M. M. Nielsen, K. Bechgaard, B. M. W. Langeveld-Voos, A. J. H. Spiering, R. A. J. Janssen, E. W. Meijer, P. Herwig, D. M. de Leeuw, *Nature*, 1999, **401**, 685-688.

18 S. Berson, R. De Bettignies, S. Bailly, S. Guillerez, *Adv. Funct. Mater.,* 2007, **17** (8), 1377-1384.

19 P. R. Huang, Y. He, C. Cao, Z. H. Lu, *NPG Asia Materials*, 2013, **5**, e57.

20 S. Zhou, Y. Liu, W. Hu, D. Zhu, X. Qiu, C. Wang, C. Bai, *Chem. Phys. Lett.*, 1998, **297** (1-2), 77-82

21 D. Chirvase, Z. Chiguvare, M. Knipper, J. Parisi, V. Dyakonov, J. C. Hummelen, *Synthetic Metals*, 2003, **138**, 299-304.

22 P. Eyben, T. Janssens, W. Vandervorst, *Mater. Sci. Eng. B*, 2005, 124, 45-53 and references therein.

23 M. A. Lambert, P. Mark, Current injection in solids, *Academic Press, New York*, **1970**.

24 H. Yang, E. Glynos, B. Huang, P. F. Green, *Phys. Chem. C*, 2013, **117** (19), 9590-9597.

25 J. Schafferhans, A. Baumann, A. Wagenpfahl, C. Deibel, *Org. Elec.*, 2010, **11**, 1693-1700.

26 P. Pingel, R. Schwarzl, D. Neher, *Appl. Phys. Lett*., ***2012***, **100**, 143303.

27 J. J. Brondijk, F. Maddalena, K. Asadi, H. J. van Leijen, M. Heeney, P. W. M. Blom, D. M. de Leeuw, *Phys. Status Solidi B*, 2012, **249**, 138-141.